

Helioseismic Modeling of Background Flows

ANDREY M. STEJKO,¹ ALEXANDER G. KOSOVICHEV,¹ AND NAGI N. MANSOUR²

¹*New Jersey Institute of Technology
323 Dr Martin Luther King Jr Blvd.
Newark, NJ 07012, USA*

²*University of Illinois at Urbana-Champaign
104 S Wright St.
Urbana, IL 61801, USA*

(Received –; Revised –; Accepted –)

Submitted to ApJ

ABSTRACT

We present a 3-dimensional (3D) numerical solver of the linearized compressible Euler equations (GALE – Global Acoustic Linearized Euler), used to model acoustic oscillations throughout the solar interior. The governing equations are solved in conservation form on a fully global spherical mesh ($0 \leq \phi \leq 2\pi$, $0 \leq \theta \leq \pi$, $0 \leq r \leq R_\odot$) over a background state generated by the standard Solar Model S. We implement an efficient pseudo-spectral computational method to calculate the contribution of the compressible material derivative dyad to internal velocity perturbations, computing oscillations over arbitrary 3D background velocity fields. This model offers a foundation for a “forward-modeling” approach, using helioseismology techniques to explore various regimes of internal mass flows. We demonstrate the efficacy of the numerical method presented in this paper by reproducing observed solar power spectra, showing rotational splitting due to differential rotation, and applying local helioseismology techniques to measure travel times created by a simple model of single-cell meridional circulation.

Keywords: Helioseismology, Computational Methods, Solar meridional circulation

1. INTRODUCTION

Since the first measurements of 5-minute solar oscillations nearly 60 years ago (Leighton et al. 1962; Claverie et al. 1979) helioseismology has evolved into a rich and diverse field using surface observations to probe solar depths, inferring solar parameters and dynamics. Comprehensive overviews of helioseismology can be found in Christensen-Dalsgaard (2002); Di Mauro (2003); Gizon & Birch (2005). The global nature of these oscillations has allowed for some of the most precise measurements of the solar interior that are currently available and have become an indispensable tool in measuring internal solar rotation (Duvall et al. 1984; Schou et al. 1998) and meridional circulation (Giles et al. 1997; Zhao & Kosovichev 2004).

The nature of Solar rotation is a complex problem and carries with it important information on the dynamic structure of the Sun. Accurate modeling of internal rotation is vital to understanding effects that rapid rotation rates and angular momentum transport can play in internal mixing of elements and hence, the evolution of solar structure. Observations of the solar surface show a pattern of differential rotation (Snodgrass & Ulrich 1990) which varies widely in its period at the equator (~ 24 days) to near the poles (~ 30 days). This pattern of differential rotation is mimicked throughout the convective interior (upper 30% of the solar radius), with a slight maximum in the velocity of subsurface layers ($\sim 0.95R_\odot$). These rates begin to converge at the tachocline (Kosovichev 1996) where the differential rotation is coupled to a solid core rotating at rate of ~ 430 nHz. Even though helioseismology has

made unprecedented strides in modeling interior solar dynamics, many unanswered questions remain. Inversion results near the poles show some discrepancies between the Global Oscillation Network Group (GONG) and the Michelson Doppler Imager (MDI) (Schou et al. 2002) data pipelines as well as newer HMI (Howe et al. 2011) observations. There are also conflicting measurements of the solar core’s rotation rate using low-degree modes ($l = 1 - 4$) – ranging from significantly lower rates (BiSON, Chaplin et al. (1996)) to much higher ones (IRIS, Lazrek et al. (1996)). Recent measurements of g-modes have also implied rotation rates more than twice as fast as previous estimates (Fossat et al. 2017).

Perpendicular to global rotation, we see strong poleward flows (20 m s^{-1}) in each hemisphere (Hathaway 1996). These meridional mass flows operate as mechanisms that distribute angular momentum and magnetic flux throughout the convective interior (Hathaway et al. 2003). Techniques in local helioseismology use perturbations in acoustic travel times to observe these flows (Gizon & Birch 2005), however it becomes more difficult to clearly resolve structures at greater depths. There is still no consensus on the nature and location of the return flow of meridional circulation cells – while commonly thought to sit in the relatively deep region at the base of the tachocline (Giles 1999), new techniques and measurements have begun to question this assumption (Mitra-Kraev & Thompson 2007; Hathaway 2012). The structure of these circulation cells has also been put to doubt, with recent measurements inferring more than just a single cell per hemisphere (Zhao et al. 2013), cf. Gizon et al. (2020).

Through persistent uncertainties on the nature of solar structure, forward-modeling offers an important avenue for the validation and systematic analysis of the helioseismology techniques used to infer internal solar parameters. Numerical acoustic solar models have been instrumental in testing these techniques under approximate solar conditions; since the seminal work of Jensen et al. (2003), simulating subsurface sound speed perturbations (Parchevsky & Kosovichev 2007; Parchevsky et al. 2014), 3D cartesian models of the solar atmosphere have been employed to validate local time-distance measurements in regimes of convection (Braun et al. 2007) and magnetic fields (Cameron et al. 2008; Khomenko et al. 2009; Parchevsky & Kosovichev 2009a,b; Felipe et al. 2016). The limitations of the computational domains, needed to probe deeper structures, led to the development of global spherical models (Hanasoge et al. 2006, 2007; Hartlep et al. 2008, 2013; Papini et al. 2015; Gizon et al. 2017) – providing key validations of inversion techniques and inferred observations of sound speed perturbations and background flow structures in the hydrodynamic regime. These models have provided a strong basis for evaluating mean flow structures on the Sun – providing support (Hartlep et al. 2013) for the inference of a double-cell (Zhao et al. 2013; Chen 2019) meridional velocity profiles in HMI observations; however, with recent inferences that reaffirm the single-cell structure (Gizon et al. 2020) on MDI and GONG data, it becomes clear that a detailed systematic investigation of these techniques and the limits of resolving internal structures is required. In order to address some of these issues we demonstrate the efficacy of a new pseudo-spectral global acoustic algorithm – developed to quickly and flexibly compute stochastically excited oscillations over wide varieties of static or dynamic 3-dimensional background velocity fields. Such fully global solar simulations have the potential to offer insights on global effects of complex hydrodynamic structures in the solar interior – from modeling meridional circulation and center-to-limb effects (Chen 2019) to exploring the information that g-modes carry about the rotating solar core. The computational techniques presented in this paper will also become the basis for adding linear contributions of global magnetic field terms in future work.

This paper is organized as follows: in §2 we describe the mathematical background and computational set-up of the model. In §3 we detail the specific numerical methods we used to compute our governing equations. In §4 we reproduce the solar p-mode spectrum and frequency splitting due to differential rotation. We continue our validation by reproducing measurements of a simple single-cell model of meridional circulation using local helioseismology techniques in §5. Finally, we discuss future plans for the model and state our concluding remarks in §6.

2. MODEL DESCRIPTION

2.1. Mathematical Background

In this section we present the mathematical formulation and computational set-up for the GALE (Global Acoustic Linearized Euler) code – a 3-dimensional numerical solver of the linearized compressible Euler equations, used to model acoustic oscillations throughout the solar interior. For the sake of simplicity we assume the adiabatic approximation, where the time-scale of heat transfer is much smaller than the period of oscillations and is therefore neglected in the

conservation of energy (Christensen-Dalsgaard 2014). The governing equations are solved on a fully global spherical mesh, $0 \leq \phi \leq 2\pi$, $0 \leq \theta \leq \pi$, $0 \leq r \leq R_\odot$, in the Cauchy conservation form; they are enumerated as follows:

$$\frac{\partial \rho'}{\partial t} + \Upsilon' = 0, \quad (1)$$

$$\frac{\partial \Upsilon'}{\partial t} + \nabla : (\mathbf{m}'\tilde{\mathbf{u}} + \tilde{\rho}\tilde{\mathbf{u}}\mathbf{u}') = -\nabla^2(p') - \nabla \cdot (\rho'\tilde{g}_r\hat{\mathbf{r}}) + \nabla \cdot S\hat{\mathbf{r}}, \quad (2)$$

$$\frac{\partial p'}{\partial t} = -\frac{\Gamma_1\tilde{p}}{\tilde{\rho}} \left(\nabla \cdot \tilde{\rho}\mathbf{u}' + \rho'\nabla \cdot \tilde{\mathbf{u}} - \frac{p'}{\tilde{p}}\tilde{\mathbf{u}} \cdot \nabla\tilde{\rho} + \tilde{\rho}\mathbf{u}' \cdot \frac{N^2}{g}\hat{\mathbf{r}} \right). \quad (3)$$

In Eqns. (1)-(3), we solve for oscillations in the potential field (ϕ) independently, and solenoidal contributions are discarded, here Υ is defined as the divergence of the momentum field \mathbf{m} ($\Upsilon = \nabla \cdot \mathbf{m} = \nabla \cdot \rho\mathbf{u} = \nabla^2\phi$). ρ , u , p , g are the density, velocity, pressure and gravity terms respectively. Γ_1 is the adiabatic ratio, constant in time in the adiabatic approximation. The full derivation for current form of the energy equation (Eq. 3) can be found in Appendix A. The governing equations are linearized - split into a base flow (tilde) and a perturbation from that base flow (prime), and only the 1st order correlation terms are considered; the base values are derived from a theoretical background state - the standard solar model S (Christensen-Dalsgaard et al. 1996). N^2 is the Brunt-Väisälä frequency where

$$N^2 = g \left(\frac{1}{\Gamma_1} \frac{\partial \ln p}{\partial r} - \frac{\partial \ln \rho}{\partial r} \right). \quad (4)$$

Our set of linear equations become unconditionally unstable in regions where this term is negative ($N^2 < 0$). These instabilities can be avoided by deriving the conservation of energy (Eq. 3) as a function of the Brunt-Väisälä frequency, allowing us to set slightly negative values in the convection zone to zero directly, without the need to alter background profiles of pressure, density or the adiabatic ratio (Γ_1) as in similar convectively stable models of Hanasoge et al. (2006); Parchevsky & Kosovichev (2007); Hartlep et al. (2008). Altering the algorithm to maintain stability may introduce small deviations from the original model (Papini et al. 2014), but is accurate enough to be used in testing helioseismology techniques throughout the convection zone.

The formulation of the source function ($S\hat{\mathbf{r}}$) is similar to that of Hanasoge et al. (2006), where a thin shallow layer bounded by the model surface (R_\odot) simulates the source of solar oscillations, see Goldreich et al. (1994), Stein & Nordlund (2001). This function is modeled as a radial Gaussian with a standard deviation of $\sigma = 0.0001R_\odot \sim 69.6$ km and centered at $\mu = 0.9995R_\odot$ - simulating radial force perturbations from the solar surface. The full time-dependent spectrum of the source is generated in frequency space with a Gaussian function centered at $\mu = 3.2$ mHz and with a standard deviation of $\sigma = 1$ mHz - simulating the power peak of observed solar oscillations. To mimic a stochastic excitation of our modes (Woodard 1984), we multiply our temporal Gaussian function by a set of random numbers at each frequency interval ($f_s = 1/\Delta t$); subsequently applying a Fourier transform to produce a randomized oscillating function for our source, of which a unique one is created for every harmonic degree and azimuthal order (l, m) in our spherical harmonic decomposition.

The material derivative ($\nabla : (\mathbf{m}'\tilde{\mathbf{u}} + \tilde{\rho}\tilde{\mathbf{u}}\mathbf{u}')$) is solved in its conservation form in order to fully account for effects that background velocities exert on the conservation of momentum (Eq. 2) in the acoustic regime. This is an important requirement for properly simulating effects of differential rotation and meridional circulation on the frequency of solar oscillations.

2.2. Radial Grid

The radial grid is spaced evenly with respect to acoustic travel time ($\int 1/c_s dr$) in order to compute acoustic oscillations across the large variations in sound speed (c_s) throughout the model. While this grid is effective at capturing effects throughout most of the model interior, as we move towards the surface ($r > 0.99R_\odot$) pressure and density scale heights begin to drop off faster than sound speed. In order to resolve the effect of the Brunt-Väisälä frequency (N^2), we switch to a logarithmic pressure grid spaced evenly in $\ln(p)$ (Hanasoge et al. 2006). Above the model surface ($r > R_\odot$), we implement a thin isothermal buffer layer with constant grid spacing up to $r = 1.001R_\odot$.

2.3. Boundary Conditions

The boundary layers are solved as simple reflective walls with a zero velocity perturbation condition ($\mathbf{u}' = 0$). To avoid non-physical surface reflections from affecting our solution, we implement a buffer layer by placing a damping factor (σ) into our governing equations:

$$\frac{\partial \rho'}{\partial t} = -\Upsilon' - \sigma \rho' , \quad \frac{\partial \Upsilon'}{\partial t} = -\nabla^2 p' + \mathcal{Y} - \sigma \Upsilon' , \quad \frac{\partial p'}{\partial t} = \mathcal{P} - \sigma p' . \quad (5)$$

To avoid precision errors from our damping term, it is computed implicitly in our time-discretization scheme using the integrating factor method. Damping is initiated at the model surface (R_\odot) and steadily increased into the atmospheric layers, mimicking the escape of acoustic oscillations above the cutoff frequency (> 5 mHz).

3. NUMERICAL METHOD

The time-discretization scheme used in governing Eqns. (1)-(3) is the 2nd order accurate ($\mathcal{O}(h^2)$) Adams-Bashforth method – used to compute the effect of external contributions of background fields to our conservation of momentum and conservation of energy (Eqns. 2 - 3) considerations, denoted by \mathcal{Y} and \mathcal{P} in Eq. (5) respectively. To advance our continuity and conservation of momentum forward in time ($\rho'(\Upsilon'), \Upsilon'(p')$), (Eqns. 1 - 2), we use the implicit 1st order accurate ($\mathcal{O}(h)$) backward Euler method – helping to maintain the stability of our solution.

Spatial differentiation in the radial direction employs the 2nd order accurate central finite-difference scheme (Eq. 6) when computing the radial component of the Laplacian (∇^2) in Eq. 2:

$$\frac{\partial}{\partial r} \left(r^2 \frac{\partial f}{\partial r} \right) = \frac{2}{\Delta r_k + \Delta r_{k+1}} \left(r_{k+0.5}^2 \frac{f_{k-1} - f_k}{\Delta r_{k+1}} - r_{k-0.5}^2 \frac{f_k - f_{k-1}}{\Delta r_k} \right) , \quad (6)$$

where subscript k denotes separate radial mesh points and Δr_k represents the radial distance between points $k-1$ and k . The computation of the 1st radial derivative also employs a 2nd order accurate polynomial central finite-difference scheme (Fig. 7).

$$\frac{\partial f}{\partial r} = -\frac{\Delta r_{k+1}}{\Delta r_k(\Delta r_{k+1} + \Delta r_k)} f_{k-1} + \frac{\Delta r_{k+1} - \Delta r_k}{\Delta r_{k+1} \Delta r_k} f_k + \frac{\Delta r_k}{\Delta r_{k+1}(\Delta r_{k+1} + \Delta r_k)} f_{k+1} . \quad (7)$$

The precision of these techniques and their agreement with theoretical calculations of eigenmodes is quite high (Fig. 1) – serving well to validate the computational techniques used in this algorithm; higher order accurate schemes may improve our results, but in the large variations in our non-uniform radial regime, many of the improvements that we expect may be greatly diminished.

Differentiation tangent to the sphere is done in the pseudo-spectral regime through spherical harmonic decomposition using the Libsharp spherical harmonic library (Reinecke & Seljebotn 2013). Tangential resolution is defined by the maximum allowable quantum number ($l_{max}(r)$) at each radial point. This value controls the mesh size of our Gauss-Legendre grid, containing $N_\phi = 3l_{max}$ azimuthal grid points and $N_\theta = 3l_{max}/2$ latitudinal grid points. These values are chosen to avoid aliasing during spherical harmonic decomposition. The azimuthal mesh points (N_ϕ) are spaced at even intervals between $0 < \phi < 2\pi$, while the latitudinal points (N_θ) are placed at the roots of the corresponding Legendre Polynomial between $0 < \theta < \pi$. To avoid oversampling at high latitudes the Libsharp library natively implements polar optimisation, or the “reduced Gauss-Legendre grid”.

To compute the tangential components of the divergence we use vector and tensor spherical harmonic bases (VSH and TSH) to calculate our terms spectrally, as defined in §3.1 and §3.2 respectively.

3.1. Vector Spherical Harmonics

Using the “pure-spin” vector spherical harmonic (VSH) components defined by Thorne (1980), we can expand an arbitrary vector field (\mathbf{E}) into the following linearly independent basis.

$$\mathbf{E} = \sum_{m=-lmax}^{lmax} \sum_{l=|m|}^{lmax} \left(E_{lm}^r(r) \mathbf{Y}_{lm} + E_{lm}^{(1)}(r) \mathbf{\Psi}_{lm} + E_{lm}^{(2)}(r) \mathbf{\Phi}_{lm} \right) , \quad (8)$$

where E_{lm}^r is the radial vector component, and $E_{lm}^{(1)}$, $E_{lm}^{(2)}$ are components tangential to the surface of the 2-sphere. Transformations between the spherical coordinate basis and our VSH basis is achieved by a set of functions defined in Novak et al. (2010), and computed using recurrence relations of the spherical harmonic (Y_{lm}). We define the divergence of our vector field (\mathbf{E} in Eq. 8) in our new basis with Eq. (9).

$$\nabla \cdot \mathbf{E} = \sum_{m=-lmax}^{lmax} \sum_{l=|m|}^{lmax} \left(\frac{dE_{lm}^r}{dr} + \frac{2}{r} E_{lm}^r - \frac{l(l+1)}{r} E_{lm}^{(1)} \right) Y_{lm} \quad (9)$$

The radial derivative is computed using the finite-difference method described in §3.

3.2. Tensor Spherical Harmonics

The tensor spherical harmonic (TSH) basis is built on groups 0 and 2 of the irreducible representation of rotation in $SO(3)$ (\mathcal{D}^0 , \mathcal{D}^2 where $t = \mathcal{D}^0 + \mathcal{D}^1 + \mathcal{D}^2$), which correspond to the trace and the symmetric traceless tensor respectively (Mathews 1962). This basis is coupled with spin-0 and spin-2 spherical harmonics to form 6 irreducible representations of a symmetric tensor, which can be rearranged into the “pure-spin tensor harmonics” defined by Zerilli (1970) and Thorne (1980). We can use these components to expand an arbitrary symmetric tensor (\mathbf{t}) into the following orthogonal basis (Novak et al. 2010).

$$\mathbf{t} = \sum_{m=-lmax}^{lmax} \sum_{l=|m|}^{lmax} \left(L_{lm}^0 \mathbf{T}_{lm}^{\mathbf{L}0} + E_{lm}^1 \mathbf{T}_{lm}^{\mathbf{E}1} + B_{lm}^1 \mathbf{T}_{lm}^{\mathbf{B}1} + T_{lm}^0 \mathbf{T}_{lm}^{\mathbf{T}0} + E_{lm}^2 \mathbf{T}_{lm}^{\mathbf{E}2} + B_{lm}^2 \mathbf{T}_{lm}^{\mathbf{B}2} \right), \quad (10)$$

where L_{lm}^0 is the fully radial component (t^{rr}) and T_{lm}^0 is the transverse ($t^{\theta\theta}$, $t^{\phi\phi}$) portion of the trace. E_{lm}^1 and B_{lm}^1 represent the mixed radial/transverse components ($t^{r\theta}$, $t^{r\phi}$), and E_{lm}^2 and B_{lm}^2 are symmetric transverse traceless components. We can use this basis to solve for the divergence of a tensor in spherical coordinates, where

$$\nabla \cdot \mathbf{t} = \begin{cases} [\nabla \cdot \mathbf{t}]_{lm}^r Y_{lm} = \sum_{m=-lmax}^{lmax} \sum_{l=|m|}^{lmax} \left[\frac{1}{r^2} \frac{\partial}{\partial r} (r^2 L_{lm}^0) - \frac{1}{r} (l(l+1) E_{lm}^1 + T_{lm}^0) \right] Y_{lm}, \\ [\nabla \cdot \mathbf{t}]_{lm}^{(1)} Y_{lm} = \sum_{m=-lmax}^{lmax} \sum_{l=|m|}^{lmax} -l(l+1) \left[\frac{1}{r^3} \frac{\partial}{\partial r} (r^3 E_{lm}^1) + \frac{1}{r} \left(\frac{T_{lm}^0}{2} - (l-1)(l+2) E_{lm}^2 \right) \right] Y_{lm}, \\ [\nabla \cdot \mathbf{t}]_{lm}^{(2)} Y_{lm} = \sum_{m=-lmax}^{lmax} \sum_{l=|m|}^{lmax} -l(l+1) \left[\frac{1}{r^3} \frac{\partial}{\partial r} (r^3 B_{lm}^1) - \frac{(l-1)(l+2)}{r} B_{lm}^2 \right] Y_{lm}. \end{cases} \quad (11)$$

Coordinate transformations between the spherical, VSH and TSH bases is done using relations defined in Novak et al. (2010). We can plug the results of this computation into Eq. (9) to compute the divergence dyad ($\nabla \cdot$) in our material derivative (Eq. 2).

4. MODEL VALIDATION

In order to validate the mathematical set-up (§2) and computational techniques (§3) described in this paper, we start by matching the generated power spectrum from our model with a theoretical prediction computed using the standard solar model S (§4.1). We test the computation of our material derivative (Eq. 2) in two simple regimes of background velocity flows: differential rotation (§4.2) and a single-cell model of meridional circulation (§5).

The parameters used in this validation are as follows: the surface resolution of the model is set by a spherical harmonic degree of $l_{max} = 200$, corresponding to $N_\phi = 600$ longitudinal and $N_\theta = 450$ latitudinal mesh points. These values are chosen in order to fully resolve the acoustic modes that intersect the base of the tachocline (a depth of $\sim 0.70R_\odot$) – letting us infer flows from any point in the convective interior using local helioseismology techniques (Gizon & Birch 2005). Our simulation is run for a period of 65 hours model time. This is too short to properly resolve flow velocities on the order of those seen in meridional circulation ($\sim 14 \text{ m s}^{-1}$). In order to achieve a desirable signal-to-noise ratio in our validation of meridional circulation measurements, we increase the magnitude of our meridional velocity by a factor of 36, to a maximum of 500 m s^{-1} – simulating an SNR that would be observed over ~ 9.5 yrs, approaching the decade minimum that is estimated to be needed in order to resolve deep meridional flows (Braun & Birch 2008).

4.1. Power Spectrum

Acoustic oscillations on the solar surface, can be decomposed into eigenmodes of radial velocity ($u'_r \hat{\mathbf{r}}$), representing standing waves throughout the solar interior. These modes can be conceptualized as a combination of the scalar spherical harmonic (Y_{lm}) with a frequency dependent radial order (ξ_n),

$$u'_r(r, \theta, \phi, t) = \sum_{n,l} \sum_{m=-l}^l \xi_n(r) Y_{lm}(\theta, \phi) e^{i\omega t}. \quad (12)$$

The power spectrum of these modes can be visualized using an $l - \nu$ diagram, showing continuous radial modes throughout the solar interior as a function of their frequency ($\omega = 2\pi\nu$) and spherical harmonic degree (l), Fig. 1. The eigenmodes are excited in the frequency range determined by our source function (S , see §2.1). By setting negative values of the Brunt-Väisälä frequency to zero we remove the convective instabilities that act as sources of acoustic perturbations normally seen below 2 mHz. We see an agreement in the structure of the eigenmodes generated by our model to theoretical calculations from the model S (Christensen-Dalsgaard et al. 1996), denoted by the dashed blue lines in Fig. 1.

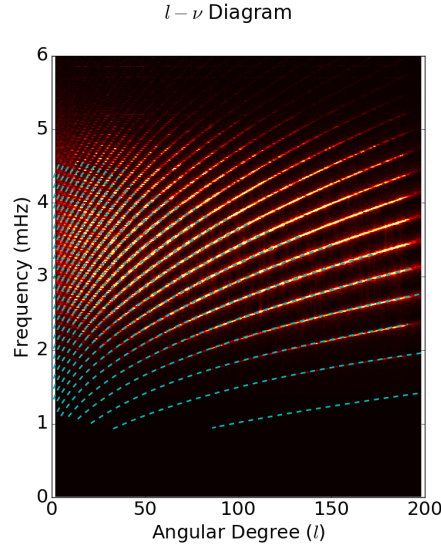


Figure 1. An $l - \nu$ diagram, showing the power spectrum of p-modes sampled 20 km above the model surface. Blue dashed lines represent theoretical predictions of eigenmodes made by the standard solar model S (Christensen-Dalsgaard et al. 1996).

4.2. Rotation

In order to test the computation of our material derivative (Eq. 2), we implement a simple model of differential rotation in a non-rotating reference frame by defining our background velocity term as the angular frequency (Ω) derived from the mean-field model M1 described in Pipin & Kosovichev (2019) and shown in Fig. 2.

This simple azimuthal velocity flow field model creates easily detectable rotational splitting in the structure of our eigenmodes. The rotational profile will shift up the frequency of prograde modes and shift down the frequency of retrograde modes as a function of their azimuthal order (m). In order to visualize this shift we can use an $m - \nu$ diagram of the power spectrum for spherical harmonic degree $l = 180$ (Fig. 3), where our simulated modes reproduce the characteristic tilt due to the average rotation along with the curvature created by the differential rotation in the convection zone. The blue dashed lines show frequency splittings calculated using helioseismic sensitivity kernels (Schou et al. 1998) for the M1 model (Pipin & Kosovichev 2019).

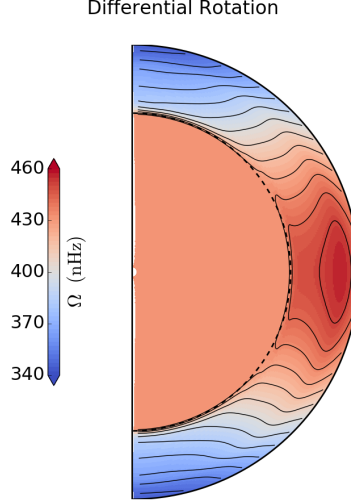


Figure 2. The angular frequency (Ω) profile derived from model M1 described in Pipin & Kosovichev (2019), showing differential rotation in the convection zone ($0.70R_{\odot} - 1.001R_{\odot}$) with a solid rotating core ($< 0.70R_{\odot}$).

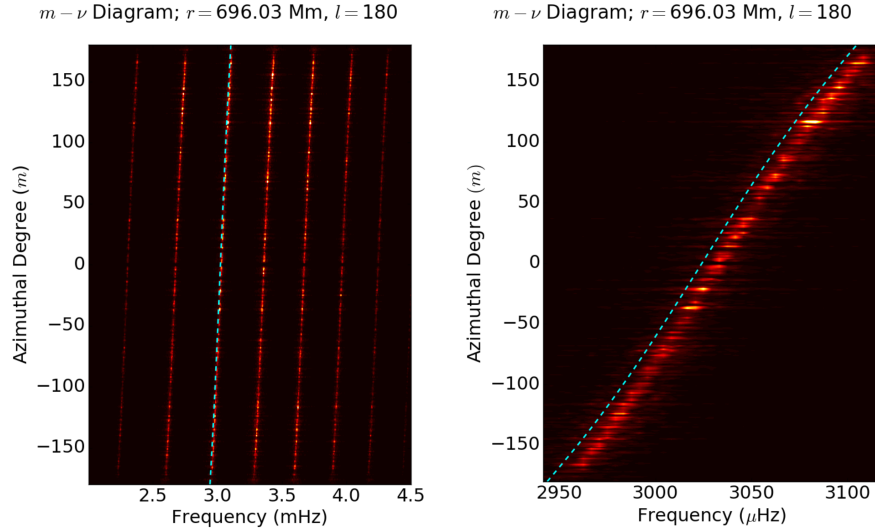


Figure 3. An $m - \nu$ diagram, showing the power spectrum of acoustic oscillation sampled 30 km above the model surface, for spherical harmonic degree $l = 180$. Blue dashed lines represent frequency splittings calculated using helioseismic sensitivity kernels (Schou et al. 1998) for the M1 model (Pipin & Kosovichev 2019).

5. MERIDIONAL CIRCULATION

The computation of our material derivative (Eq. 2) can be tested in a regime of global meridional flows by using a simple single-cell model of meridional circulation as our background velocity term ($\tilde{\mathbf{u}}$, Fig. 5). We chose the model described and tested by Hartlep et al. (2013), recreating their measurements as a simple validation of our computational techniques.

In order to infer flows in the model interior using surface measurements, we apply a method of deep focusing (Zhao et al. 2009) – a local helioseismology technique (for an in-depth review, see Gizon & Birch (2005)) which uses travel times of acoustic waves to probe structures in solar and stellar interiors. This method consists of choosing two points on the model surface, separated by some angular distance (Δ); the signals at these points are cross-correlated, measuring acoustic travel times of internal oscillations (p-modes). As these waves travel through the resonant cavity of the

convective interior they are advected by internal mass flows. Sampling waves traveling in opposite directions results in travel time differences ($\delta\tau$) which provide a basis for inferring background velocities. The ray path approximation under the assumption of Fermat's principle offers a simple relation between these values (Giles 1999).

$$\delta\tau = -2 \int_{\Gamma_0} \frac{\tilde{\mathbf{u}} \cdot \mathbf{n}}{c^2} ds. \quad (13)$$

Travel time differences can be estimated along the unperturbed ray path (Γ_0).

We employ this technique to infer meridional velocities by measuring travel time differences between southward and northward traveling waves ($\delta\tau_{NS}$). Using each pixel in our data set as a center point, we remap the surrounding $60^\circ \times 60^\circ$ patch into azimuthal equidistant coordinates (Postel's projection) using cubic hermite splines. The remapped resolution is approximately 0.6° per pixel, the same spatial resolution as our Gauss-Legendre grid (§3). An illustration of our method can be seen in Fig. 4.

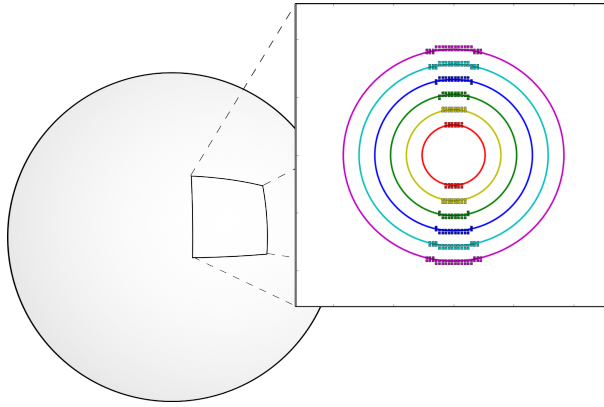


Figure 4. An illustration of pixel selection for our deep-focusing method. A $60^\circ \times 60^\circ$ patch is remapped into azimuthal equidistant coordinates to a resolution of approximately 0.6° per pixel. Six concentric circles are selected at diameters $\Delta = 12^\circ, 18^\circ, 24^\circ, 30^\circ, 36^\circ$ and 42° . Pixels are chosen in 30° wide northern and southern sectors two pixels in width.

A series of six concentric great circles are drawn at diameters of $\Delta = 12^\circ, 18^\circ, 24^\circ, 30^\circ, 36^\circ$ and 42° . Sets of pixels (two pixels in width) are selected along the rings in 30° wide northern and southern sectors. The pixels in each sector are averaged together and the signals in opposing sectors are cross-correlated. This process is repeated for every grid point in our model (N_ϕ, N_θ) and the cross-correlated signal is averaged over every point in the longitude (N_ϕ) and $\pm 3^\circ$ (± 5 px. in N_θ) in the latitude. To further smooth our data, we average the diameter of each great circle over $\pm 2.4^\circ$ – travel times of the varying diameter distances are interpolated to an estimated time offset based on ray path theory (Giles 1999). The radial turning points of acoustic waves corresponding to each angular distance are $\sim 0.93, 0.89, 0.85, 0.81, 0.77, 0.72 R_\odot$ respectively, allowing us to probe the entirety of the convective interior. In Fig. 5 we show the meridional flow profile used in the model with dashed lines in the upper hemisphere corresponding to the ray paths for each great circle.

5.1. Results

The travel time differences ($\delta\tau_{NS}$) for each ring diameter are plotted as a function of latitude in Fig. 6. These values are compared to theoretical travel time differences (dashed lines in Fig. 6) computed using the ray path approximation (Eq. 13) employing the standard solar model S (Christensen-Dalsgaard et al. 1996).

The travel time differences for all ring diameters show solid agreement with theoretical predictions as well as the analysis of Hartlep et al. (2013). These results show a key validation of the numerical procedure used to compute the model as well as the deep focusing techniques used to analyze the data. The error (σ_{NS}) is calculated using a separate model with no background flows; this reference model uses an identical source function (S , Eq. 2) and analysis sequence, producing the same error profile we see for each ring diameter (Fig. 6). We characterize this error as the

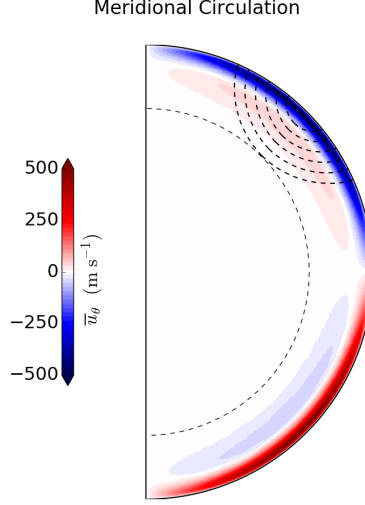


Figure 5. The latitudinal velocity (\tilde{u}_θ) of a single-cell model of meridional circulation (Hartlep et al. 2013). The dashed lines represent ray paths of acoustic oscillations (p-modes) between diameters of $\Delta = 12^\circ, 18^\circ, 24^\circ, 30^\circ, 36^\circ$ and 42° with radial turning points at depths: $\sim 0.93, 0.89, 0.85, 0.81, 0.77, 0.72 R_\odot$ respectively.

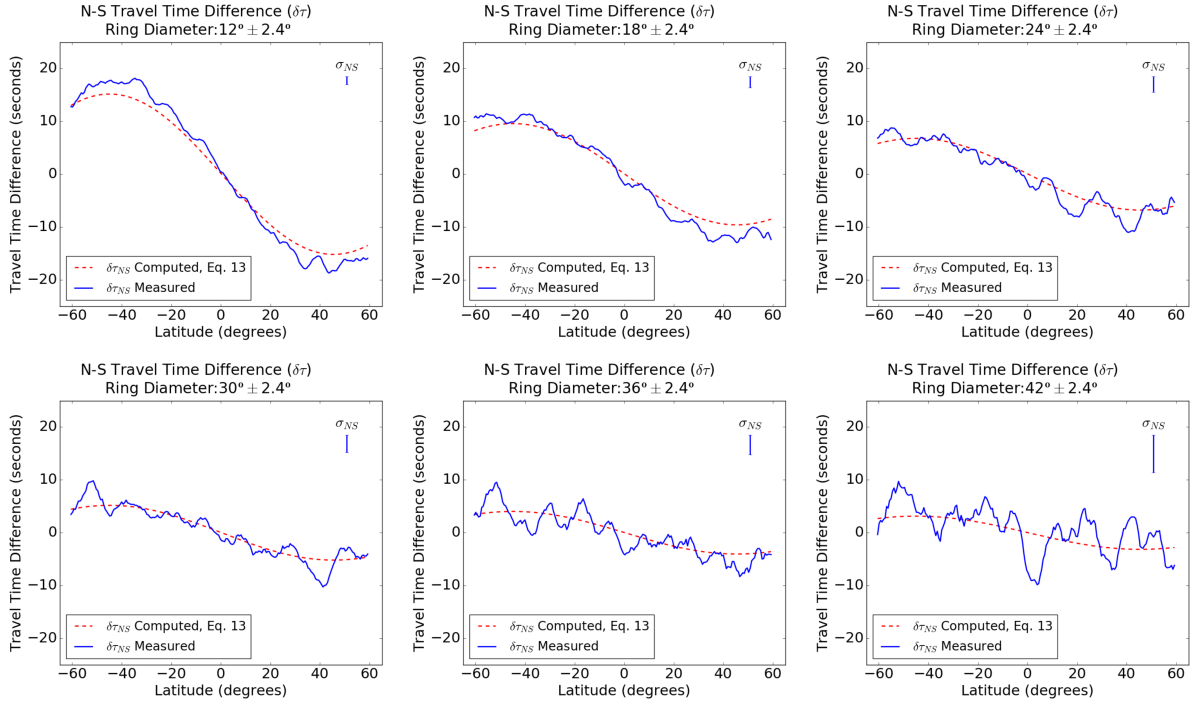


Figure 6. The N-S travel-time differences (δt_{NS}) as a function of latitude for six depths: $\sim 0.93, 0.89, 0.85, 0.81, 0.77, 0.72 R_\odot$ corresponding to travel distances of $\Delta = 12^\circ, 18^\circ, 24^\circ, 30^\circ, 36^\circ$ and 42° respectively. The signal is averaged over $\pm 3^\circ$ in latitude and $\pm 2.4^\circ$ in travel distance.

standard deviation of travel time differences ($\delta\tau$) from zero in our reference model, taking the RMS over latitudinal grid points.

$$\sigma_{NS} = \sqrt{\frac{1}{N} \sum_{i=1}^N \delta\tau_i^2}. \quad (14)$$

The characteristic noise profiles seen in models without flows can be subtracted from measured travel-time differences (Fig. 6) in order to remove some of the most significant impacts of realization noise on our measurements (Hanasoge et al. 2007). This method of attenuating noise can provide us an opportunity to compare measurements made by computational helioseismology to estimates of the ray-path approximation. The resulting NS travel-time profile can be found in Appendix B, Fig. 9.

In order to further increase the SNR in our measurements we apply a phase speed filter, defined by a Gaussian function with a width of $\sigma = 0.05v_p$, where $v_p = \omega/L$ is the phase speed (Nigam et al. 2007). After the application of this filter, the travel time differences display high levels precision but do show a latitude-independent systematic offset for different ring diameters. This offset, which seems to have a maximum of approximately ± 1 s (Fig. 7), is a characteristic of the realization noise in our model and can be removed by subtracting the phase-filtered noise profile for the same model with no background flows. The resulting profiles, which can be found in Appendix B, Fig. 10, show remarkable agreement with predictions made using the ray-path approximation (Eq. 13), implying that non-linear effects do not seem to have dramatic impacts on our measurements of travel times.

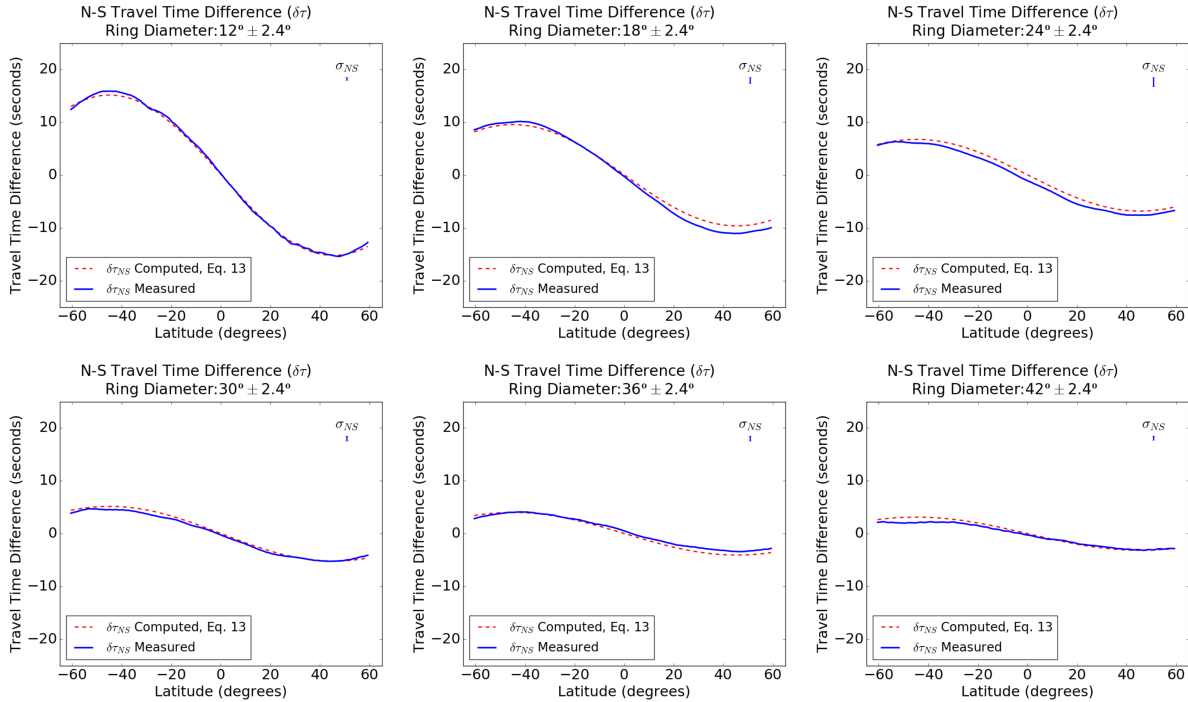


Figure 7. The N-S travel-time differences ($\delta\tau_{NS}$) under the application of a Gaussian phase speed filter ($\sigma = 0.05v_p$) as a function of latitude for six depths: $\sim 0.93, 0.89, 0.85, 0.81, 0.77, 0.72 R_\odot$ corresponding to travel distances of $\Delta = 12^\circ, 18^\circ, 24^\circ, 30^\circ, 36^\circ$ and 42° respectively. The signal is averaged over $\pm 3^\circ$ in latitude and $\pm 2.4^\circ$ in travel distance.

The error function (σ_{NS} , Eq. 14) provides a solid foundation for the characterization of realization noise at various acoustic travel depths. We show the error as a function of travel distance (Δ) in Fig. 8, along with travel time differences ($\delta\tau$) from our reference model without background flows for 5 separate latitudinal averages ($30^\circ\text{N} - 50^\circ\text{N}$, $10^\circ\text{N} - 30^\circ\text{N}$, $10^\circ\text{S} - 10^\circ\text{N}$, $10^\circ\text{S} - 30^\circ\text{S}$, $30^\circ\text{S} - 50^\circ\text{S}$) and compare them with the error in the unfiltered signal (Fig. 6). The cause of the apparent systematic error is unclear, however, the latitude-dependent offset profiles are strongly linked to the structure of our source (S , Eq. 2), with different random number seeds generating different error profiles. This effect deserves its own systematic investigation for varying parameters of source locations and structures.

In Fig. 8, we see a similar systematic error structure in both the filtered and unfiltered signals. As we move towards greater depths, however, noise in the unfiltered signal grows significantly, concealing any potential offset. These results may have interesting implications for measuring meridional flow structures at the base of the tachocline. The application of our phase speed filter seems to have preserved signal quality relatively evenly throughout the convection zone, offering encouraging results for probing flows deep in the solar interior.

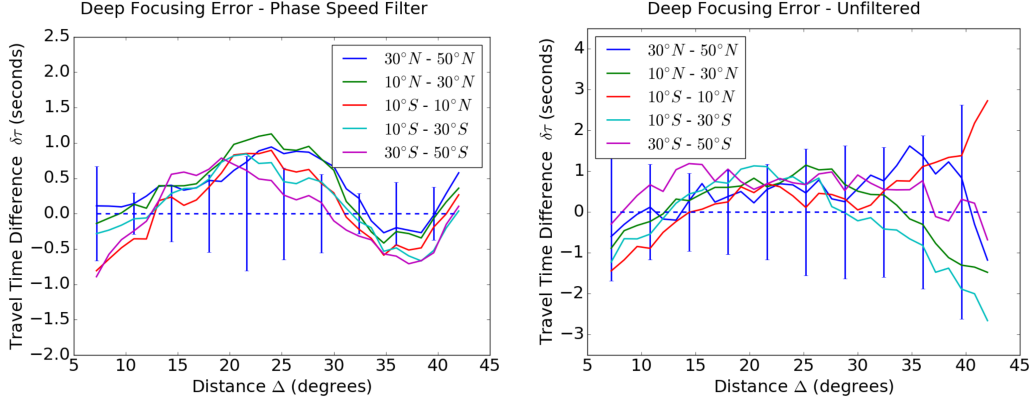


Figure 8. The error in travel time differences ($\delta\tau$) as a function of travel distance (Δ) for 5 latitudinal averages spanning $30^\circ\text{N} - 50^\circ\text{N}$, $10^\circ\text{N} - 30^\circ\text{N}$, $10^\circ\text{S} - 10^\circ\text{N}$, $10^\circ\text{S} - 30^\circ\text{S}$, $30^\circ\text{S} - 50^\circ\text{S}$. Error bars show the standard deviation of the measured offset (σ_{NS} , Eq. 14) across the entire latitude. Left) Error for data analyzed with a Gaussian phase speed filter ($\sigma = 0.05v_p$). Right) Error for unfiltered signal.

6. DISCUSSION

We present a global linearized acoustic algorithm with new computational methods that will facilitate the testing and validation of local and global helioseismology techniques in diverse regimes of 3-dimensional flows. While helioseismology has been an indispensable tool in exploring interior dynamics on the Sun, it can have trouble resolving exact profiles of flow, especially at greater depths. Forward modeling offers the opportunity to test the impact of subtle differences generated by a variety of theoretical models of mean mass flows, forming a basis to better interpret observational oscillation data.

The model is validated for two distinct profiles: differential rotation and meridional circulation. These two regimes are critical for understanding and simulating the distribution of angular momentum and magnetic flux that governs the solar magnetic cycle. To simulate these structures, we present an application of pseudo-spectral techniques which will be necessary components for future models to efficiently compute spherical harmonic resolutions of $l_{max} > 300$, previously considered to be too computationally expensive. These resolutions will be necessary to model local helioseismology techniques on sound speed perturbations due to small-scale structures on the solar surface, creating a link to linear effects of global perturbations.

In future work, we plan to use this model to test differences in acoustic travel-time signatures between models of one and two-cell meridional circulation. The current state surrounding the nature of meridional velocity profiles remains uncertain, with similar techniques producing widely varying results between observational data from HMI (Zhao et al. 2013) and MDI/GONG (Gizon et al. 2020). While both studies employed validation through the use of forward-modeling, the theoretical profiles of meridional circulation structures for one and two-cell models varied extremely. A new efficient and flexible code presents a timely opportunity to run a differential study on much more subtle differences between one and two-cell circulation models – for both theoretical profiles as well as ones derived from solar simulations. Our investigation (Stejko, Kosovichev, in preparation) will explore subtle differences in flow velocities near the base of the tachocline, focusing on the limits what can be resolved within the two-decade long window of current solar observations, with and without preparing data using phase-speed filtering. These models will be used for an analysis of realization noise in simulations of stochastic excitations of surface oscillations – for large numbers source profiles and measurement times. This level of systematic investigation will provide a baseline for what can be interpreted from observational data. In further work, we also plan to create a new generation of models that include linear effects of magnetic field structures on acoustic oscillations. The numerical method demonstrated in this paper will be the basis for computing this effect.

AMS would like to thank the heliophysics modeling and simulation team at NASA Ames Research Center for very productive meetings. This work is supported by the NASA grants: 80NSSC19K0630, 80NSSC19K1436, NNX14AB7CG and NNX17AE76A.

REFERENCES

- Braun, D. C., Birch, A. C., Benson, D., Stein, R. F., Nordlund, Å. 2007, *ApJ*, 669, 1395
- Braun, D. C., Birch, A. C. 2008, *ApJ*, 689, 161
- Cameron, R., Gizon, L., Duvall, T. L., Jr. 2008, *SoPh*, 251, 291
- Chaplin, W. J., Elsworth, Y., Isaak, G. R., et al. 1996, *MNRAS*, 283, 31
- Chen, R. 2019, Ph.D. Thesis, Stanford University
- Christensen-Dalsgaard, J., Dappen, W., Ajukov, S. V. 1996, *Sci*, 272, 1286
- Christensen-Dalsgaard, J., 2002, *RvMP*, 74, 1073
- Christensen-Dalsgaard, J., 2014, D.f.I.Print, Aarhus.
- Claverie, A., Isaak, G. R., McLeod, C. P., van der Raay, H. B., Cortes, T. R. 1979, *Nature*, 282, 591
- Di Mauro, M. P. 2003, *LNP*, 599, 31
- Duvall, T. L., Jr., Dziembowski, W. A., Goode, P. R., et al. 1984, *Nature*, 310, 22
- Felipe, T., Braun, D. C., Crouch, A. D., Birch, A. C. 2016, *ApJ*, 829, 67
- Fossat, E., Boumier, P., Corbard, T., et al. 2017, *A&A*, 604, 40
- Giles, P. M., Duvall, T. L., Scherrer, P. H., Bogart, R. S. 1997, *Nature*, 390, 52
- Giles, P. M. 1999, Ph.D. Thesis, Stanford University
- Gizon, L., Birch, A. C. 2005, *LRSP*, 2, 6
- Gizon, L., Barucq, H., Duruflé, M. 2017, *A&A*, 600, 35
- Gizon, L., Cameron, R. H., Pourabadian, M., et al. 2020, *Sci*, 368, 1469
- Goldreich, P., Murray, N., Kumar, P. 1994, *ApJ*, 424, 466
- Hanasoge, S. M., Larsen, R. M., Duvall, T. L., Jr., et al. 2006, *ApJ*, 648, 1268
- Hanasoge, S. M., Duvall, T. L., Jr., Couvidat, S. 2007, *ApJ*, 664, 1234
- Hartlep, T.; Zhao, J., Mansour, N. N.; Kosovichev, A. G. 2007, *ApJ*, 689, 1373
- Hartlep, T., Zhao, J., Kosovichev, A. G., Mansour, N. N. 2013, *ApJ*, 762, 132
- Hathaway, D. H. 1996, *ApJ*, 460, 1027
- Hathaway, D. H., Nandy, D., Wilson, R. M., Reichmann, E. J. 1996, *ApJ*, 589, 665
- Hathaway, D. H. 2012, *ApJ*, 760, 84
- Howe, R., Larson, T. P., Schou, J., et al. 2011, *JPhCS*, 271, 2061
- Jensen, J. M., Olsen, K. B., Duvall, T. L., Jr., Jacobsen, B. H. 2003, *ESASP*, 517, 319
- Khomenko, E., Kosovichev, A. G., Collados, M., Parchevsky, K., Olshevsky, V. 2009, *ApJ*, 694, 411
- Kosovichev, A. G. 1996, *ApJ*, 469, 61
- Lazrek, M., Pantel, A., Fossat, E., et al. 1996, *SoPh*, 166, 1
- Leighton, R. B., Noyes, R. W., Simon, G. W. 1962, *ApJ*, 135, 474
- Mathews, J. 1962, *SIAM*, 10, 768
- Mitra-Kraev, U., Thompson, M. J. 2007, *Astron.Nachr.*, 328, 1009
- Nigam, R., Kosovichev, A. G., Scherrer, P. H. 2007, *ApJ*, 659, 1736
- Novak, J., Cornou, J. -L., Vasset, N. 2010, *CoPh*, 229, 399
- Papini, E.; Gizon, L.; Birch, A. C. 2014, *SoPh*, 289, 1919
- Papini, E., Birch, A. C., Gizon, L., Hanasoge, S. M. 2015, *A&A*, 577, 145
- Parchevsky, K. V., Kosovichev, A. G. 2007, *ApJ*, 666, 547
- Parchevsky, K. V., Kosovichev, A. G. 2009, *ApJ*, 694, 573
- Parchevsky, K. V., Kosovichev, A. G. 2009, *ASPC*, 416, 61
- Parchevsky, K. V., Zhao, J., Hartlep, T., Kosovichev, A. G. 2014, *ApJ*, 785, 40
- Pipin, V. V., Kosovichev, A. G. 2019, *ApJ*, 887, 215
- Reinecke, M., Seljebotn, D. S. 2013, *A&A*, 554, 112
- Schou, J., Antia, H. M., Basu, S., et al. 1998, *ApJ*, 505, 390
- Schou, J., Howe, R., Basu, S., et al. 2002, *ApJ*, 567, 1234
- Snodgrass, H. B., Ulrich, R. K. 1990, *ApJ*, 351, 309
- Stein, R. F., Nordlund, Å. 2001, *ApJ*, 546, 585
- Thorne, K. S. 1980, *RvMP*, 52, 299
- Woodard, M. F. 1984, Ph.D. Thesis, University of California, San Diego
- Zerilli, F. J. 1970, *J. Math. Phys.*, 11, 2203
- Zhao, J., Kosovichev, A. G., 2004, *ApJ*, 603, 776
- Zhao, J., Hartlep, T., Kosovichev, A. G., Mansour, N. N. 2009, *ApJ*, 702, 1150
- Zhao, J., Bogart, R. S., Kosovichev, A. G., Duvall Jr., T. L., Hartlep, T. 2013, *ApJL*, 774, 29

APPENDIX

A. ENERGY EQUATION

In our formulation, we employ the adiabatic approximation, where we assume that heat transfer is negligible in the time-scale of acoustic oscillations. The relationship between pressure and density in this regime (see [Christensen-Dalsgaard \(2014\)](#)) can be expressed in Eulerian form as

$$\frac{\partial p}{\partial t} + \mathbf{u} \cdot \nabla p = \frac{\Gamma_1 p}{\rho} \left(\frac{\partial \rho}{\partial t} + \mathbf{u} \cdot \nabla \rho \right) . \quad (\text{A1})$$

Assuming that the adiabatic ratio (Γ_1) remains constant, we can linearize Eq. (A1) as follows, where primes denote a perturbation from a base (tilde) value.

$$\tilde{\rho} \frac{\partial p'}{\partial t} + \rho' \frac{\partial \tilde{p}}{\partial t} + (\rho' \tilde{\mathbf{u}} \cdot \nabla \tilde{p} + \tilde{\rho} (\tilde{\mathbf{u}} \cdot \nabla p' + \mathbf{u}' \cdot \nabla \tilde{p})) = \Gamma_1 \left(\tilde{p} \frac{\partial \rho'}{\partial t} + p' \frac{\partial \tilde{\rho}}{\partial t} + (p' \tilde{\mathbf{u}} \cdot \nabla \tilde{\rho} + \tilde{p} (\tilde{\mathbf{u}} \cdot \nabla \rho' + \mathbf{u}' \cdot \nabla \tilde{\rho})) \right) . \quad (\text{A2})$$

In order to avoid convective instabilities in our model we can rewrite Eq. (A2) in terms of the Brunt-Väisälä frequency (N^2 , Eq. 4). By plugging in Continuity (Eq. 1) and rearranging terms, we are left with:

$$\frac{1}{\tilde{\rho} \Gamma_1} \frac{\partial p'}{\partial t} + \frac{1}{\tilde{\rho}} \nabla \cdot (\tilde{\rho} \mathbf{u}' + \rho' \tilde{\mathbf{u}}) = -\mathbf{u}' \cdot \left(\frac{1}{\Gamma_1 \tilde{\rho}} \nabla \tilde{p} - \frac{1}{\tilde{\rho}} \nabla \tilde{\rho} \right) - \tilde{\mathbf{u}} \cdot \left(-\frac{1}{\tilde{\rho}} \left(\nabla \rho' + \frac{p'}{\tilde{p}} \nabla \tilde{\rho} \right) \right) . \quad (\text{A3})$$

Substituting (N^2 , Eq. 4) and rearranging terms further leaves us with the final form of our governing relation for pressure (Eq. 3).

$$\frac{\partial p'}{\partial t} = -\frac{\Gamma_1 \tilde{p}}{\tilde{\rho}} \left(\nabla \cdot \tilde{\rho} \mathbf{u}' + \rho' \nabla \cdot \tilde{\mathbf{u}} - \frac{p'}{\tilde{p}} \tilde{\mathbf{u}} \cdot \nabla \tilde{\rho} + \tilde{\rho} \mathbf{u}' \cdot \frac{N^2}{g} \hat{\mathbf{r}} \right) . \quad (\text{A4})$$

B. REMOVING NOISE

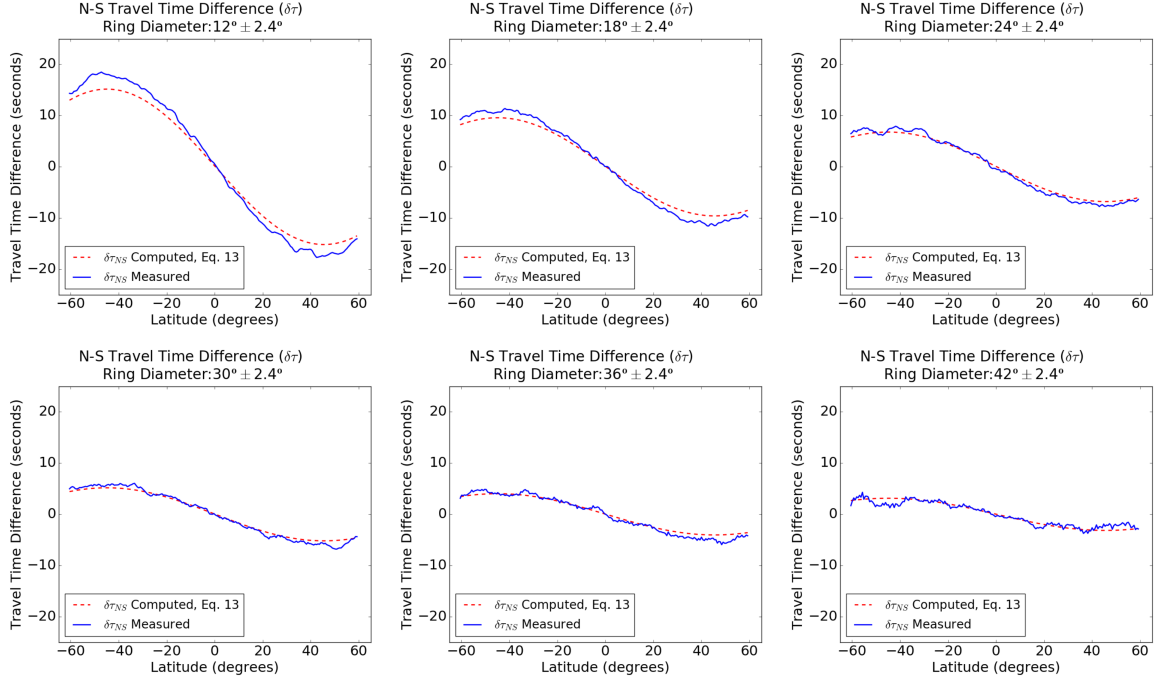


Figure 9. The N-S travel-time differences (δt_{NS}) with noise subtracted from corresponding model with no flows. The travel-times are plotted as a function of latitude for six depths: $\sim 0.93, 0.89, 0.85, 0.81, 0.77, 0.72 R_{\odot}$ corresponding to travel distances of $\Delta = 12^{\circ}, 18^{\circ}, 24^{\circ}, 30^{\circ}, 36^{\circ}$ and 42° respectively. The signal is averaged over $\pm 3^{\circ}$ in latitude and $\pm 2.4^{\circ}$ in travel distance.

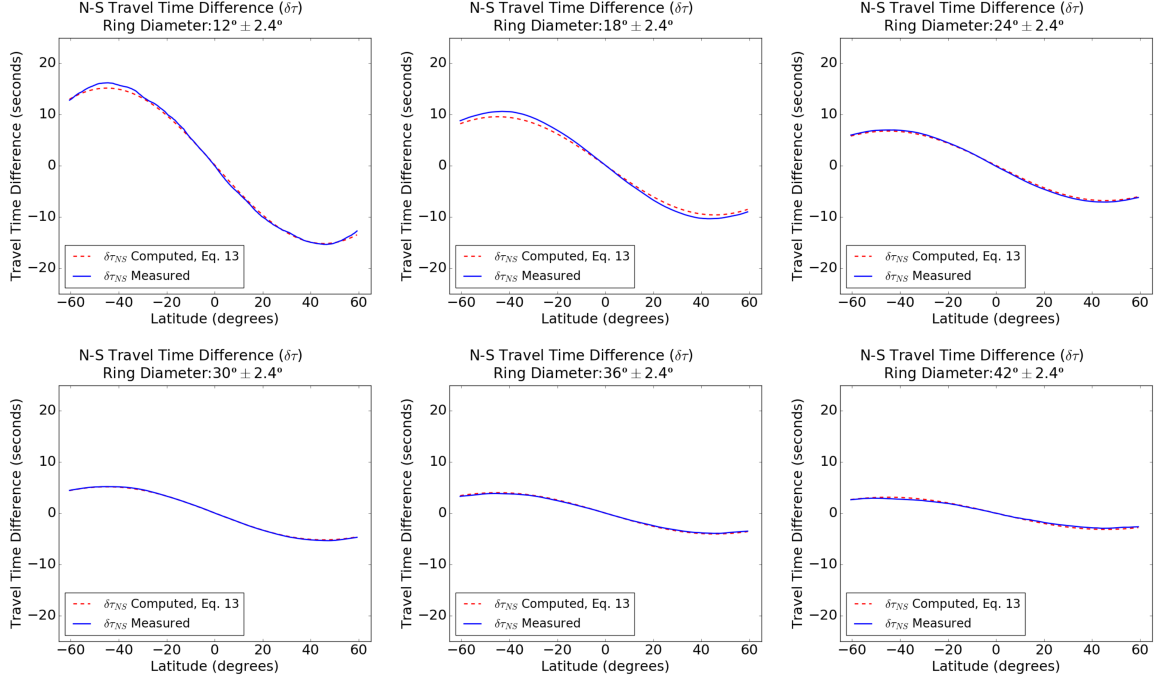


Figure 10. The N-S travel-time differences (δt_{NS}) under the application of a Gaussian phase speed filter ($\sigma = 0.05v_p$) with noise subtracted from corresponding model with no flows. The travel-times are plotted as as a function of latitude for six depths: $\sim 0.93, 0.89, 0.85, 0.81, 0.77, 0.72 R_{\odot}$ corresponding to travel distances of $\Delta = 12^{\circ}, 18^{\circ}, 24^{\circ}, 30^{\circ}, 36^{\circ}$ and 42° respectively. The signal is averaged over $\pm 3^{\circ}$ in latitude and $\pm 2.4^{\circ}$ in travel distance.